ARMY RESEARCH LABORATORY

Two-Scale Modelling of Effects of Microstructure and Thermomechanical Properties on Dynamic Performance of an Aluminium Alloy

by J. D. Clayton

ARL-RP-300 **September 2010**

**A reprint from the *Int. J. Materials and Structural Integrity*,
Vol. 4, Nos. 2/3/4, pp. 116–140, 2010.**

NOTICES

Disclaimers

The findings in this report are not to be construed as an official Department of the Army position unless so designated by other authorized documents.

Citation of manufacturer's or trade names does not constitute an official endorsement or approval of the use thereof.

Destroy this report when it is no longer needed. Do not return it to the originator.

Army Research Laboratory

Aberdeen Proving Ground, MD 21005-5066

ARL-RP-300 **September 2010**

Two-Scale Modelling of Effects of Microstructure and Thermomechanical Properties on Dynamic Performance of an Aluminium Alloy

J. D. Clayton

Weapons and Materials Research Directorate, ARL

A reprint from the *Int. J. Materials and Structural Integrity*, Vol. 4, Nos. 2/3/4, pp. 116–140, 2010.

REPORT DOCUMENTATION PAGE

Form Approved
OMB No. 0704-0188

1. REPORT DATE *(DD-MM-YYYY)*	2. REPORT TYPE	3. DATES COVERED (From - To)
September 2010	Reprint	October 2007–January 2010

4. TITLE AND SUBTITLE
Two-Scale Modelling of Effects of Microstructure and Thermomechanical Properties on Dynamic Performance of an Aluminium Alloy

5a. CONTRACT NUMBER

5b. GRANT NUMBER

5c. PROGRAM ELEMENT NUMBER

6. AUTHOR(S)
J. D. Clayton

5d. PROJECT NUMBER
AH80

5e. TASK NUMBER

5f. WORK UNIT NUMBER

7. PERFORMING ORGANIZATION NAME(S) AND ADDRESS(ES)
U.S. Army Research Laboratory
ATTN: RDRL-WMP-B
Aberdeen Proving Ground, MD 21005-5066

8. PERFORMING ORGANIZATION REPORT NUMBER
ARL-RP-300

9. SPONSORING/MONITORING AGENCY NAME(S) AND ADDRESS(ES)

10. SPONSOR/MONITOR'S ACRONYM(S)

11. SPONSOR/MONITOR'S REPORT NUMBER(S)

12. DISTRIBUTION/AVAILABILITY STATEMENT
Approved for public release; distribution is unlimited.

13. SUPPLEMENTARY NOTES
A reprint from the *Int. J. Materials and Structural Integrity*, Vol. 4, Nos. 2/3/4, pp. 116–140, 2010.

14. ABSTRACT
Influences of microstructure and properties of an aluminium alloy on resistance to dynamic perforation are predicted using a decoupled multi-scale modelling approach. At the scale of individual grains, a crystal plasticity model is developed accounting for finite elastic and plastic deformations, thermal softening and energy storage mechanisms linked to microscopic residual stress fields induced by line defects and second-phase particles. An averaging scheme is invoked to compute macroscopic stress-deformation responses corresponding to various microstructures. The results of the averaging process motivate choices of parameters entering a macroscopic plasticity model, with different parameter sets corresponding to different microstructures. This macroscopic model, with various parameter sets, is in turn used to simulate impact and perforation of a thin plate of the aluminium alloy by a cylindrical projectile. The results provide quantitative assessments of possible benefits of texturing, insertion of strengthening and energy storage mechanisms and enhancement of ductility on performance of the alloy.

15. SUBJECT TERMS
aluminium, precipitates, texture, crystal plasticity, impact, ballistics, multi-scale modolling

16. SECURITY CLASSIFICATION OF:			17. LIMITATION OF ABSTRACT	18. NUMBER OF PAGES	19a. NAME OF RESPONSIBLE PERSON
a. REPORT	b. ABSTRACT	c. THIS PAGE			J. D. Clayton
Unclassified	Unclassified	Unclassified	UU	32	19b. TELEPHONE NUMBER (*Include area code*) 410-278-6146

Two-scale modelling of effects of microstructure and thermomechanical properties on dynamic performance of an aluminium alloy

J.D. Clayton

Impact Physics, RDRL-WMP-B,
US Army Research Laboratory,
Aberdeen Proving Ground, MD 21005-5066, USA
E-mail: jclayton@arl.army.mil

Abstract: Influences of microstructure and properties of an aluminium alloy on resistance to dynamic perforation are predicted using a decoupled multiscale modelling approach. At the scale of individual grains, a crystal plasticity model is developed accounting for finite elastic and plastic deformations, thermal softening and energy storage mechanisms linked to microscopic residual stress fields induced by line defects and second-phase particles. An averaging scheme is invoked to compute macroscopic stress-deformation responses corresponding to various microstructures. The results of the averaging process motivate choices of parameters entering a macroscopic plasticity model, with different parameter sets corresponding to different microstructures. This macroscopic model, with various parameter sets, is in turn used to simulate impact and perforation of a thin plate of the aluminium alloy by a cylindrical projectile. The results provide quantitative assessments of possible benefits of texturing, insertion of strengthening and energy storage mechanisms and enhancement of ductility on performance of the alloy.

Keywords: crystal plasticity; aluminium; multi-scale modelling; ballistics.

Reference to this paper should be made as follows: Clayton, J.D. (2010) 'Two-scale modelling of effects of microstructure and thermomechanical properties on dynamic performance of an aluminium alloy', *Int. J. Materials and Structural Integrity*, Vol. 4, Nos. 2/3/4, pp.116-140.

Biographical notes: J.D. Clayton is a member of the scientific staff at the US Army Research Laboratory. He has authored a number of publications in areas of physical, mathematical, computational and engineering sciences.

1 Introduction

Considered here is the dynamic thermomechanical response of a monolithic metallic plate fabricated from a precipitate-strengthened aluminium alloy. The alloy of study is Al 2139, consisting primarily of elemental Al and containing smaller amounts of Cu, Mg, Ag, Mn and trace amounts of Si and Fe (Cho and Bes, 2006). The heterogeneous polycrystalline microstructure exhibited by this material is representative of the general class of Al-Cu-Mg-Ag alloys. The material exhibits a face centred cubic (FCC) crystal structure at room temperature and low pressures, and consists of bulk grains and

secondary phases that emerge upon processing either within grains or preferentially near grain boundaries. These secondary phases may include Ω (chemical composition Al_2Cu) that nucleates homogeneously throughout the alloy, contributes to hardening without facilitating grain boundary fracture (Cho and Bes, 2006), and in fine distributions leads to creep resistance and superior strength (Hutchinson et al., 2001). Also in such alloys, without the addition of Ag or with the addition of Zr, the phase denoted θ' (also of chemical composition Al_2Cu) emerges, often along grain boundaries and promoting intergranular fracture. Dispersoids of Mn are also common. Such particles, when very small, may increase ductility by promoting mobile dislocation generation (Vasudevan et al., 1986), but larger Mn particles can act as stress risers and may be detrimental (Brown and Stobbs, 1971).

Aluminium alloys of various compositions have been the focus of numerous numerical studies relevant to the present work. Povrik et al. (1995) developed a crystal plasticity model incorporating thermal effects to describe thin film aluminium interconnects. Hanim and Klepaczko (1999) implemented a macroscopic continuum theory to model spall fracture in an aluminium alloy. Starink et al. (1999) described effects of precipitates, ceramic inclusions, dislocations, point defects, chemical compositions, grain sizes and subgrain sizes on the mechanical behaviour of Al-Li-Cu-Mg alloys using a scalar-based phenomenological model. Gall et al. (2000) studied the effects of particle cluster morphology on fracture and particle-matrix debonding in a cyclically loaded cast Al-Si alloy. Cheng and Itoh (2004) conducted simulations of ballistic impact of thick Al 7039 plates using macroscopic plasticity and failure models. Zhao et al. (2004) modelled surface roughening in aluminium sheets under both uniaxial and biaxial tension using a computational crystal plasticity approach. Dwivedi et al. (2006) modelled shock compression of polycrystalline aluminium microstructures featuring a variety of microstructural features such as hardened or softened grain boundaries, porosity and ceramic inclusions. Rezvanian et al. (2006) studied evolution of dislocation cells in aluminium undergoing severe plastic deformation using a dislocation-based crystal plasticity model. Wu et al. (2006) modelled grain boundary damage and shear localisation across multiple grains of a polycrystalline Al-Cu-Mg alloy.

A limited number of experiments have been conducted to assess ductility, fracture strength and high-rate behaviour of the Al 2139 alloy (Cho and Bes, 2006; Ravichandran, 2007). Specifically, the alloy exhibits a tensile elongation in excess of 0.15, a room temperature fracture toughness on the order of 200 MPa $m^{1/2}$, and an ultimate tensile strength on order of 500 MPa. At high compressive strain rates ($10^3 – 10^4$/s), the material exhibits relatively little rate dependence on flow stress, with a maximum flow stress on the order of 800 MPa and ductility in excess of 0.5, though thermal softening is evident at compressive strains exceeding 0.35. Observations also suggest that the material is relatively resistant to failure by adiabatic shear localisation. Preliminary experiments (Cho and Bes, 2006; Cheeseman, 2007) have indicated promise with regards to resistance of plates of the alloy to dynamic penetration.

Crystal plasticity theory is used in the present approach to address effects of microstructure – specifically rolling textures (Randle and Engler, 2000; Wenk and Van Houtte, 2004), slip system strengthening rate and residual elastic energy (Taylor and Quinney, 1934; Rosakis et al., 2000) on the dynamic elastic-plastic response of the alloy. In a related work, Schoenfeld and Kad (2002) used crystal plasticity theory to study

effects of crystallographic texture on the high-rate shear response of a Ti-6Al-4V alloy. Schoenfeld and Kad (2002) found that lattice orientations affect the overall shear strength of the metal as well as the evolution of localisation deformation modes, and suggested that the most shear-resistant textures, i.e., those with highest macroscopic shear strength and with delayed adiabatic shear localisation, should be the most resistant to dynamic perforation. Computational complexity presently limits 3-D crystal plasticity predictions to domains on the order of 1 mm^3 or smaller when individual grain geometries are fully resolved (Becker, 2004). This limitation renders simulations of impact events with specimens of realistic spatial dimensions unfeasible. As such, an averaging procedure (Taylor, 1938; Kalidindi et al., 1992) is used here to deduce the effective thermomechanical properties of an aggregate of crystals, and then these results are used to calibrate macroscopic model parameters entering simulations of high-speed impact. Of course, many microstructural details are lost when the polycrystalline geometry is not fully resolved, including some elements of anisotropy, neighbouring grain interactions, shear band propagation across individual grains and discrete intra- and intergranular fractures. But such effects can in part be reflected implicitly via choice of macroscopic thermodynamic and kinetic material parameters, giving what is deemed here a reasonably realistic depiction of the polycrystalline response to high-rate shear deformation. The peripheral shear stress along the lateral impactor-target interface is often deemed the dominant resistive stress component in the plugging stages of perforation (Schoenfeld and Kad, 2002), specifically plug formation, plug separation and plug slipping (Li and Goldsmith, 1996). It is noted that some uncertainty is inevitably inherent in the present performance predictions, however, as a result of the limitations imposed by the relative simplicity of purely macroscopic depictions of inelasticity and failure.

The present study interfaces aspects of materials design and structural analysis, making efficient use of limited experimental data on material behaviour and dynamic performance. The two-scale method provides quantitative bounds on performance that may be expected via conceivable adjustments of the alloy's microstructure. The remainder of this paper is organised as follows. Section 2 discusses the single crystal plasticity formulation used for microstructure scale modelling of precipitate-hardened Al alloys. Section 3 discusses the polycrystal model obtained via averaging of the single crystal response, and numerical results obtained from the crystal model. Section 4 presents the macroscopic plasticity formulation, with parameters selected following careful consideration of the aforementioned crystal plasticity results. Section 5 presents simulations of impact and perforation of the Al plate. Conclusions follow in Section 6.

The following notational scheme is used. Scalars and individual components of vectors and tensors are written in italic font, while vectors and tensors are written in bold font. The summation convention applies on repeated indices, with 3-D Cartesian coordinates implied. The $\bullet$ symbol denotes the scalar product of vectors $\left(\mathbf{a}\bullet\mathbf{b} = a^a b_a = a^1 b_1 + a^2 b_2 + a^3 b_3\right)$, while juxtaposition of second rank tensors implies summation over one set of adjacent indices $\left[(\mathbf{AB})^{a}_{.c} = A^{ab} B_{bc}\right]$. Summation over two sets of adjacent indices is denoted by the **:** symbol $\left(\mathbf{A} : \mathbf{B} = A^{ab} B_{ab}\right)$. Superposed $\bullet$, T and -1 denote the material time derivative, transpose and matrix inversion operations, respectively. Additional notation is explained as it appears.

2 Single crystal plasticity

The crystal plasticity theory implemented here follows the general thermodynamic framework developed for single crystals of cubic symmetry by Clayton (2005a, 2005b), where more detailed descriptions and physical justifications for most modelling assumptions can be found. The framework is further extended here to encompass variability in properties attributed to second-phase inclusions in Al-Cu-Mg-Ag alloys. The second-phase particles of interest here, on the order of tens to hundreds of nanometres in diameter, are deemed too small relative to the dimensions of the Al grains, on the order of tens to hundreds of microns in size, to resolve explicitly and distinctly from the bulk grains. Instead, their effects are assumed to enter parameters controlling kinetics of individual slip systems (Kocks et al., 1975) and mechanisms of energy storage (Taylor and Quinney, 1934; Rosakis et al., 2000) attributed to stress concentrations of blocked dislocations and pile-ups at phase boundaries, for example. Because precise values of such parameters have yet to be quantified experimentally for the present class of alloys, parametric studies over realistic ranges of values are conducted, ultimately enabling description of effects of strain hardening rate and stored energy on dynamic performance in impact events.

Let $\mathbf{x} = \mathbf{x}(\mathbf{X}, t)$ represent a smooth time-dependent motion, with $\mathbf{x}$ and $\mathbf{X}$ denoting spatial and reference coordinates, respectively, of a material particle. Deformation gradient $\mathbf{f}$ is decomposed multiplicatively as:

$$\mathbf{f} = \partial \mathbf{x} / \partial \mathbf{X} = \mathbf{f}^{\mathbf{e}}\mathbf{f}^{\boldsymbol{\theta}}\mathbf{f}^{\mathbf{p}}, \tag{1}$$

where $\mathbf{f}$, $\mathbf{f}^{\boldsymbol{\theta}}$ and $\mathbf{f}^{\mathbf{p}}$ describe, respectively, kinematics of elasticity and rigid-body rotation, stress-free thermal expansion or contraction, and the cumulative irreversible contribution of moving crystal defects. In general, none of $\mathbf{f}^{\mathbf{e}}$, $\mathbf{f}^{\boldsymbol{\theta}}$ or $\mathbf{f}^{\mathbf{p}}$ is integrable. Elastic and thermal deformations dictate the kinematics of the slip direction vectors $\mathbf{s}^{(\alpha)}$ and slip plane normal covariant vectors $\mathbf{m}^{(\alpha)}$:

$$\mathbf{s}^{(\alpha)} = \mathbf{f}^{\mathbf{e}}\mathbf{f}^{\boldsymbol{\theta}}\mathbf{s}_0^{(\alpha)}\ ,\ \mathbf{m}^{(\alpha)} = \mathbf{m}_0^{(\alpha)}\mathbf{f}^{\boldsymbol{\theta}-1}\mathbf{f}^{\mathbf{e}-1}, \tag{2}$$

as illustrated in Figure 1. An additive split of spatial velocity gradient $\mathbf{l}$ follows from (1) as:

$$\mathbf{l} = \partial \dot{\mathbf{x}} / \partial \mathbf{x} = \dot{\mathbf{f}}\mathbf{f}^{-1} = \underbrace{\dot{\mathbf{f}}^{\mathbf{e}}\mathbf{f}^{\mathbf{e}-1}}_{=\mathbf{l}^{\mathbf{e}}} + \underbrace{\mathbf{f}^{\mathbf{e}}\dot{\mathbf{f}}^{\boldsymbol{\theta}}\mathbf{f}^{\boldsymbol{\theta}-1}\mathbf{f}^{\mathbf{e}-1}}_{=\mathbf{l}^{\boldsymbol{\theta}}} + \underbrace{\mathbf{f}^{\mathbf{e}}\mathbf{f}^{\boldsymbol{\theta}}\dot{\mathbf{f}}^{\mathbf{p}}\mathbf{f}^{\mathbf{p}-1}\mathbf{f}^{\boldsymbol{\theta}-1}\mathbf{f}^{\mathbf{e}-1}}_{=\mathbf{l}^{\mathbf{p}}}. \tag{3}$$

Thermal deformation of a cubic lattice is isotropic:

$$\mathbf{l}^{\boldsymbol{\theta}} = \dot{\mathbf{f}}^{\boldsymbol{\theta}}\mathbf{f}^{\boldsymbol{\theta}-1} = \alpha_T \dot{\theta}\mathbf{1}, \tag{4}$$

where θ is the temperature, α_T is the temperature-dependent thermal expansion coefficient, and unit tensor is denoted by $\mathbf{1}$. The plastic velocity gradient in the intermediate configuration $\bar{b}$ of Figure 1 is written:

$$\bar{\mathbf{l}}^{\mathbf{p}} = \dot{\mathbf{f}}^{\mathbf{p}}\mathbf{f}^{\mathbf{p}-1} = \sum_{\alpha=1}^{n} \dot{\gamma}^{(\alpha)}\mathbf{s}_0^{(\alpha)} \otimes \mathbf{m}_0^{(\alpha)}, \tag{5}$$

with $\dot{\gamma}^{(\alpha)}$ the plastic shearing rate on slip system α, n the number of potentially active slip systems, and $\otimes$ the tensor product. As a result of the orthogonality of $\mathbf{s}_0^{(\alpha)}$ and $\mathbf{m}_0^{(\alpha)}$, the accumulated plastic deformation $\mathbf{f}^{\mathbf{p}}$ is always volume-preserving.

Figure 1 Deformations, configurations and slip directors

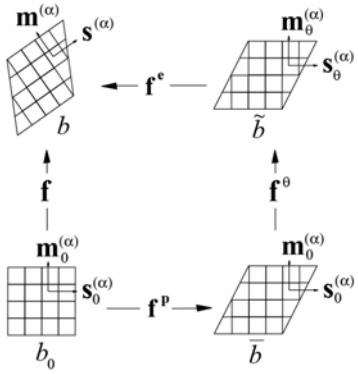

Localised balance laws are specified in the current configuration as follows:

$$\dot{\rho} + \rho\, tr\left(\mathbf{l}\right) = 0\,,\ div\boldsymbol{\sigma} + \rho\mathbf{b} = \rho\ddot{\mathbf{x}},\ \boldsymbol{\sigma} = \boldsymbol{\sigma}^T,\ \ \rho\dot{e} = \boldsymbol{\sigma} : \mathbf{l} - div\mathbf{q} + \rho r, \tag{6}$$

with ρ, $\boldsymbol{\sigma}$, $\mathbf{b}$, e, $\mathbf{q}$ and r denoting the current mass density, Cauchy stress tensor, body force vector per unit mass, internal energy per unit mass, heat flux vector per unit current area and energy source per unit mass, respectively. Here *div* is used to represent divergence with respect to spatial coordinates, and *tr* indicates the trace of a second-rank tensor. The local entropy inequality is:

$$\rho\dot{\eta} \geq -div\left(\mathbf{q}/\theta\right) + \rho r/\theta, \tag{7}$$

with $\dot{\eta}$ the rate of entropy per unit mass. Helmholtz free energy per unit mass, ψ, is:

$$\psi = e - \theta\eta. \tag{8}$$

Upon substitution of (6) and (8) into (7), the entropy inequality becomes:

$$\boldsymbol{\sigma} : \mathbf{l} - \left(\mathbf{q}\bullet\boldsymbol{\nabla}_{\mathbf{x}}\theta\right)/\theta \geq \rho\left(\dot{\psi} + \dot{\theta}\eta\right), \tag{9}$$

with $\boldsymbol{\nabla}_{\mathbf{x}}\theta$ the spatial temperature gradient.

A Helmholtz free energy potential of the following functional form is assumed:

$$\psi = \psi\left(\mathbf{e}^{\mathbf{e}}, \theta, \xi\right), \tag{10}$$

where the intermediate configuration elastic strain $\mathbf{e}^{\mathbf{e}} = (\mathbf{f}^{\mathbf{e}T}\mathbf{f}^{\mathbf{e}} - \mathbf{1})/2$. The symbol ξ denotes a dimensionless scalar internal variable representing stored micro-elastic energy associated with crystal defects (e.g., sessile dislocations) that may impede shearing on each slip system. Expanding the time derivative of (10) and inserting the result into (9):

$$\boldsymbol{\sigma} : \left(\mathbf{l}^{\mathbf{e}} + \mathbf{l}^{\mathbf{0}} + \mathbf{l}^{\mathbf{p}}\right) - (\mathbf{q} \bullet \nabla_{\mathbf{x}} \theta) / \theta \geq \rho\left(\partial_{\mathbf{e}^{\mathbf{e}}} \psi : \dot{\mathbf{e}}^{\mathbf{e}} + \left(\partial_{\theta} \psi\right)\dot{\theta} + \left(\partial_{\xi} \psi\right)\dot{\xi} + \dot{\theta}\eta\right), \tag{11}$$

where the subscript following the ∂-operator denotes partial differentiation with respect to the subscripted variable. Additional algebraic manipulations give:

$$\begin{aligned} &\frac{\rho}{\tilde{\rho}}\left(\mathbf{s}^{\mathbf{e}} - \tilde{\rho}\, \partial_{\mathbf{e}^{\mathbf{e}}} \psi\right) : \dot{\mathbf{e}}^{\mathbf{e}} + \left(\alpha_T tr\left(\boldsymbol{\sigma}\right) - \rho\left(\partial_{\theta} \psi\right) - \rho\eta\right)\dot{\theta} \\ &\qquad - \rho\left(\partial_{\xi} \psi\right)\dot{\xi} + \sum_{\alpha=1}^{n} \tau^{(\alpha)} \dot{\gamma}^{(\alpha)} \geq \mathbf{q} \bullet \nabla_{\mathbf{x}} \theta / \theta, \end{aligned} \tag{12}$$

where $\tilde{\rho}$ is the mass density in configuration $\tilde{b}$, and the elastic second Piola-Kirchhoff stress $\mathbf{s}^{\mathbf{e}} = j^{e}\mathbf{f}^{\mathbf{e}-1}\boldsymbol{\sigma}\mathbf{f}^{\mathbf{e}-T}$ with $j^{e} = det\mathbf{f}^{\mathbf{e}} = \tilde{\rho} / \rho$. The resolved Cauchy stress on slip system α is found from the definition $\tau^{(\alpha)} = \boldsymbol{\sigma} : \mathbf{s}^{(\alpha)} \otimes \mathbf{m}^{(\alpha)}$. The following relations are deduced from (12):

$$\mathbf{s}^{\mathbf{e}} = \tilde{\rho}\, \partial_{\mathbf{e}^{\mathbf{e}}} \psi, \tag{13}$$

$$\eta = \alpha_T tr\left(\boldsymbol{\sigma}\right) / \rho - \partial_{\theta} \psi = \chi - \partial_{\theta} \psi, \tag{14}$$

$$\sum_{\alpha=1}^{n} \tau^{(\alpha)} \dot{\gamma}^{(\alpha)} - \rho\left(\partial_{\xi} \psi\right)\dot{\xi} \geq \left(\mathbf{q} \bullet \nabla_{\mathbf{x}} \theta\right) / \theta. \tag{15}$$

Rearranging the last of (6) using (13) and (14) gives:

$$\rho\theta\dot{\chi} - \rho\theta\partial_{\theta}\dot{\psi} = \rho r - div\mathbf{q} + \sum_{\alpha=1}^{n} \tau^{(\alpha)} \dot{\gamma}^{(\alpha)} - \rho\left(\partial_{\xi} \psi\right)\dot{\xi}. \tag{16}$$

Specific heat capacity $\hat{c}$ is defined here as the partial derivative of the internal energy with respect to temperature at constant elastic strain and constant internal variable, i.e.:

$$\hat{c} = \partial_{\theta} e = -\theta\, \partial_{\theta\theta} \psi + \partial_{\eta} e \partial_{\theta} \chi, \tag{17}$$

where (8) has been used. Local energy balance (16) then becomes:

$$\underbrace{\rho\hat{c}\dot{\theta}}_{\substack{temperature\\ change}} = \underbrace{\sum_{\alpha=1}^{n} \tau^{(\alpha)} \dot{\gamma}^{(\alpha)}}_{\substack{plastic\\ dissipation}} - \underbrace{\rho\left(\partial_{\xi} \psi - \theta\partial_{\theta\xi} \psi\right)\dot{\xi}}_{\substack{energy\ of\\ lattice\ defects}} + \underbrace{\rho\theta\partial_{\theta\mathbf{e}^{\mathbf{e}}} \psi : \dot{\mathbf{e}}^{\mathbf{e}}}_{thermoelastic\ coupling} - \underbrace{div\mathbf{q}}_{\substack{heat\\ conduction}} + \underbrace{\rho r}_{\substack{heat\\ supply}}. \tag{18}$$

A free energy potential per unit intermediate configuration volume, deemed applicable to the class of heterogeneous alloys of study here, is now postulated as:

$$\tilde{\rho}\psi = \frac{1}{2}\mathbf{e}^{\mathbf{e}} : \mathbb{C} : \mathbf{e}^{\mathbf{e}} - \frac{1}{3}K_1\vartheta^3 + \frac{1}{2}\kappa\mu\left[\left(1 + \Omega\right)\xi\right]^2 + y, \tag{19}$$

where $\vartheta = tr(\mathbf{e}^{\mathbf{e}})$ measures the elastic volume change, $\mathbb{C}$ is the temperature dependent rank four elastic modulus, K_1 and μ are temperature dependent elastic stiffness

coefficients, and κ is a dimensionless scalar. The scalar Ω, also dimensionless, is newly introduced here to reflect effects of composition, e.g., solute atoms and/or second-phase particles in aluminium alloys, on stored energy in the bulk crystal lattice and within the precipitates themselves. Function $y = -\tilde{\rho}\hat{c}\theta\ln(\theta/\theta_0)$ accounts for thermal energy, with θ_0 a reference temperature at which $y = 0$. From (13) and (19), the stress satisfies:

$$\mathbf{s}^{\mathbf{e}} = \tilde{\rho}\,\partial_{\mathbf{e}^{\mathbf{e}}}\psi = \mathbb{C} : \mathbf{e}^{\mathbf{e}} - K_1\vartheta^2\mathbf{1}, \tag{20}$$

where the second term on the right of (20) accounts for materially nonlinear effects induced by elastic volume changes, presumably at large pressures. The hydrostatic pressure $\tilde{p}$ and deviatoric stress $\mathbf{s}^{\mathbf{e}\prime}$ in the intermediate frame then become, from (20):

$$\tilde{p} = -\frac{tr(\mathbf{s}^{\mathbf{e}})}{3} = -\frac{tr(\mathbb{C} : \mathbf{e}^{\mathbf{e}})}{3} + K_1\vartheta^2\ ,\ \mathbf{s}^{\mathbf{e}\prime} = \mathbf{s}^{\mathbf{e}} + \tilde{p}\mathbf{1} = \mathbb{C} : \mathbf{e}^{\mathbf{e}} - \left(\frac{tr(\mathbb{C} : e^{e})}{3} - K_1\vartheta^2\right)\mathbf{1}. \tag{21}$$

Kinetics of plasticity are described next. A power-law viscoplastic flow rule is used to address deformations induced by dislocation glide on each slip system:

$$\dot{\gamma}^{(\alpha)} = \dot{\gamma}_0\left(\frac{\tilde{\tau}^{(\alpha)}}{g^{(\alpha)}}\right)^m \operatorname{sgn}\left(\tilde{\tau}^{(\alpha)}\right). \tag{22}$$

Here, $\dot{\gamma}_0$ and m are material parameters, $g^{(\alpha)}$ is the slip resistance arising from dislocation barriers, $\tilde{\tau}^{(\alpha)} = j^e\tau^{(\alpha)}$ is the projected shear stress pulled back to the intermediate configuration $\tilde{b}$ of Figure 1, and $\operatorname{sgn}(x) = x/|x|$, with sgn(0) = 1. Thermal softening attributed to increased dislocation mobility at high temperatures is incorporated by the power law relation:

$$g^{(\alpha)} = g_0^{(\alpha)}\left(\theta/\theta_0\right)^p, \tag{23}$$

with $g_0^{(\alpha)}$ the flow resistance at reference temperature θ_0 and p a dimensionless constant. The following relationship between the ensemble-averaged hardening over all systems at fixed reference temperature and the internal variable ξ is used:

$$\frac{1}{n}\sum_{\alpha=1}^{n}\left(g_0^{(\alpha)} - g_y^{(\alpha)}\right) = \hat{\alpha}\mu b\sqrt{\rho_T} = \hat{\alpha}\mu\xi, \tag{24}$$

with $g_y^{(\alpha)}$ an initial yield stress, b the magnitude of the Burgers vector in the reference lattice, and ρ_T the total dislocation line length per unit intermediate configuration volume associated with shearing impedance. Scalar proportionality factor $\hat{\alpha}$ accounts for dislocation interactions. Effects of intrinsic lattice resistance to dislocation motion (e.g., Peierls barriers), as well as defects present initially in the undeformed lattice, are incorporated implicitly in the value of $g_y^{(\alpha)}$.

In FCC alloys of interest here, the number of potentially active slip systems is chosen as n = 12, with dislocation glide permitted in $\langle 110\rangle$ close-packed directions on $\{111\}$

planes. Evolution of slip resistance at reference temperature θ_0 is dictated by a hardening-minus-dynamic-recovery relation:

$$\dot{g}_0^{(\alpha)} = A(1+\Phi)\sum_{\beta=1}^{n} q_\beta^\alpha \left|\dot{\gamma}^{(\beta)}\right| - B g_0^{(\alpha)} \sum_{\beta=1}^{n} \left|\dot{\gamma}^{(\beta)}\right|, \tag{25}$$

with the interaction matrix satisfying:

$$q_\beta^\alpha = \delta_\beta^\alpha + q\left(1-\delta_\beta^\alpha\right), \tag{26}$$

where q is the latent hardening ratio. In (25), A and B are constants and Φ is a dimensionless parameter introduced here to reflect influences of alloy composition on the slip system hardening rates, since second-phase particles are thought to drastically affect strengthening in Al-Cu-Mg-Ag alloys (Hutchinson et al., 2001; Cho and Bes, 2006). In metallic crystals containing such particles, a number of mechanisms may affect the resistance to motion of individual dislocation lines (Kocks et al., 1975): friction stresses, anti-phase boundaries, misfit stresses, core and stacking fault energy differences and chemical hardening. Interfacial mechanisms at particle-matrix boundaries may lead to a flow stress dependence proportional to $\mu b c^{1/2}/w$, where c is the volume fraction of particles of width w (Kocks et al., 1975). In (25), phenomenological scaling factor Φ is applied to account for the ensemble effects of such mechanisms in Al-Cu-Mg-Ag alloys until quantitative experimental data becomes available to suggest a more descriptive formulation.

In the numerical implementation of the model, an implicit hyperelastic-viscoplastic algorithm is used to integrate the elastic-plastic constitutive response. Slip rates for a given increment spanning times t and $t + \Delta t$ are found implicitly from values of the resolved shear stress and hardening variables as:

$$\dot{\gamma}^{(\alpha)} = \dot{\gamma}_0 \left|\frac{\tilde{\tau}_{t+\Delta t}^{(\alpha)}}{g_{t+\Delta t}^{(\alpha)}}\right|^m \operatorname{sgn}\left(\tilde{\tau}_{t+\Delta t}^{(\alpha)}\right). \tag{27}$$

Notice that $\tilde{\tau}_{t+\Delta t}^{(\alpha)}$ and $g_{t+\Delta t}^{(\alpha)}$ depend upon θ through (23) and the temperature dependence of elastic moduli in (19). In an adiabatic analysis, the temperature rate for a given increment spanning t and $t + \Delta t$ is found from (18), in the absence of heat conduction or heat sources, as:

$$\dot{\theta} \approx \left(\frac{\beta}{\rho \hat{c}} \sum_{\alpha=1}^{n} \tau^{(\alpha)} \dot{\gamma}^{(\alpha)} + \frac{\theta}{\hat{c}} \partial_\theta \left(\mathbf{s}^{\mathbf{e}} : \dot{\mathbf{e}}^{\mathbf{e}} \right) \right)\Bigg|_t, \tag{28}$$

where

$$\beta = \left(\sum_{\alpha=1}^{n} \tau^{(\alpha)} \dot{\gamma}^{(\alpha)} - \rho\left(\partial_\xi \psi - \theta \partial_{\theta\xi} \psi\right)\dot{\xi} \right) \left(\sum_{\alpha=1}^{n} \tau^{(\alpha)} \dot{\gamma}^{(\alpha)} \right)^{-1}, \tag{29}$$

such that $1 - \beta$ is the ratio of the rate of stored energy to plastic dissipation.

Additional explanation regarding stored energy and the role of internal state variable ξ is now merited. Manipulating (24) followed by time differentiation gives:

$$\xi = b\sqrt{\rho_T} = \frac{\tilde{\rho}\,\partial_{\xi}\psi}{\kappa\mu\left(1+\Omega\right)^2} = \frac{1}{\hat{\alpha}\mu n}\sum_{\alpha=1}^{n}\left(g_0^{(\alpha)} - g_y^{(\alpha)}\right),\ \dot{\xi} = b\frac{\dot{\rho}_T}{2\sqrt{\rho_T}} \approx \frac{1}{\hat{\alpha}\mu n}\sum_{\alpha=1}^{n}\dot{g}_0^{(\alpha)}. \quad (30)$$

Furthermore from (19):

$$\tilde{\rho}\theta\partial_{\theta\xi}\psi = \frac{\kappa\left(1+\Omega\right)^2\theta\partial_{\theta}\mu}{\hat{\alpha}\mu n}\sum_{\alpha=1}^{n}\left(g_0^{(\alpha)} - g_y^{(\alpha)}\right). \quad (31)$$

Substituting (30) and (31) into (29) then yields:

$$\beta = 1 - \frac{\kappa\left(1+\Omega\right)^2\left(\mu+\theta\partial_{\theta}\mu\right)}{\left(\hat{\alpha}\mu n\right)^2}\left[\sum_{\alpha=1}^{n}\left(g_0^{(\alpha)} - g_y^{(\alpha)}\right)\sum_{\alpha=1}^{n}\dot{g}_0^{(\alpha)}\right]\left[\sum_{\alpha=1}^{n}\tilde{\tau}^{(\alpha)}\dot{\gamma}^{(\alpha)}\right]^{-1}. \quad (32)$$

Finally, the dislocation density variable can be determined directly from the first of (30):

$$\rho_T = \left[\frac{1}{\hat{\alpha}\mu n b}\sum_{\alpha=1}^{n}\left(g_0^{(\alpha)} - g_y^{(\alpha)}\right)\right]^2. \quad (33)$$

As is clear from (19) and (32), positive values of Ω amplify stored energy associated with internal variable ξ and equivalently, residual elastic energy engendered by microscopic stress fields manifesting from dislocation density ρ_T. Such amplification would manifest physically in Al-Cu-Mg-Ag alloys from the presence of second-phase particles of Ω, θ′ or Mn that can act as local stress risers (Brown and Stobbs, 1971) or barriers to dislocation motion. The increase in stored energy would be attributed to both elastic energy of the deforming second phases, misfit stresses (Kocks et al., 1975), as well as elastic self-energies of dislocations that may build up at phase boundaries.

Parameters entering the single crystal model, many specific to alloy Al 2139, are compiled in Table 1. Single crystalline aluminium exhibits cubic symmetry, with linear elastic constants $\mathbb{C}_{11} = \mathbb{C}^{1111}, \mathbb{C}_{12} = \mathbb{C}^{1122}$, and $\mathbb{C}_{44} = \mathbb{C}^{1212}$ obtained from Arsenlis and Parks (2002). Derivatives of elastic moduli with respect to temperature, $\partial_{\theta}\mathbb{C}$, are obtained from Hanim and Klepaczko (1999). Third-order bulk modulus constant K_1, reference mass density ρ_0, thermal expansion coefficient α_T, melting temperature θ_1, specific heat $\hat{c}$ and Burgers vector b are taken from Hatch (1984). The value of the latent hardening ratio q is obtained from Povrik et al. (1995), while $\hat{\alpha}$ follows from Zhao et al. (2004). Reference shearing rate $\dot{\gamma}_0$ and strain rate sensitivity m are obtained from Rezvanian et al. (2006), with the relatively large value of the latter reflecting little dependence of flow stress on strain rate. Reference temperature θ_0 is chosen for convenience as both the room temperature and initial temperature during adiabatic simulations. In fact, all simulations discussed later in Sections 3, 4 and 5 are adiabatic, with an initial temperature of 300 K. Adiabatic heating occurs in conjunction with plastic flow, leading to well-known thermal softening phenomena. The remaining parameters are obtained via calibration to experimental data, as explained in Section 3.

Table 1 Parameters for crystal model

Parameter	*Value*	*Parameter*	*Value*
$\mathbb{C}_{11}$	108 GPa	α	$2.3(10)^{-5} + 1.69(10)^{-8}\,\Delta\theta$/K
$\mathbb{C}_{12}$	61.3 GPa	$\hat{c}$	$900 + 0.466\,\Delta\theta$ J/kgK
$\mathbb{C}_{44}$	28.5 GPa	$g_y^{(\alpha)}$	155 MPa
$\partial_\theta \mathbb{C}_{11}$	–6.9 MPa/K	q	1.0
$\partial_\theta \mathbb{C}_{12}$	27.3 MPa/K	$\hat{\alpha}$	0.3
$\partial_\theta \mathbb{C}_{44}$	–17.1 MPa/K	b	0.2863 nm
K_1	299 GPa	$\dot{\gamma}_0$	0.001/s
ρ_0	2700 kg/m^3	m	50
$1\,\kappa$	10	A	480 MPa
θ_0	300 K	B	1.5
θ_1	933.5 K	p	–1.1

The procedure used here provides only a simple link between precipitate or defect content, stored energy of the lattice and yield strength. In the present approach, Ω and Φ are treated as adjustable scalars that affect energy storage and slip resistance in a generic manner. A more precise approach would be prescription of functional forms for Ω and Φ for the material that depend explicitly, for example, upon precipitate or dispersoid volume fractions and sizes (Kocks et al., 1975), internal (residual) lattice straining associated with chemistry and interstitial defects (Mott and Nabarro, 1948), and microscopic debonding and fracture mechanisms associated with second phases and their interfaces. Such a more precise approach will be enabled when sufficient experimental data characterising the microstructure and relevant microscopic behaviour of Al 2139 becomes available.

3 Polycrystal plasticity and homogenised response

The crystal model is calibrated to available high-rate compression data and then used to predict the high-rate shear response important in plugging stages of perforation (Li and Goldsmith, 1996; Schoenfeld and Kad, 2002). A computational algorithm is used to generate average stress-strain and temperature histories for aggregates of many grains, first in order to calibrate unknown constitutive model parameters specific to alloy Al 2139, and then to predict such histories for feasible variations in parameters associated with different processing routes. In these deformation-controlled simulations, constant velocities are prescribed on boundaries of a cube of material of unit dimensions, with this cube containing one or more grains of the material. Taylor's assumption (Taylor, 1938; Kalidindi et al., 1992) is invoked for polycrystalline simulations, meaning that $\mathbf{f}$ of (1) is identical for each grain in the aggregate throughout the time history of deformation. High strain rates are considered here, such that adiabatic conditions apply and local thermal interactions such as heat conduction between crystals are not addressed. The average Cauchy stress $\overline{\boldsymbol{\sigma}}$ is calculated for the aggregate for each time increment in the analysis

via volume averaging, assuming each crystal occupies an equal part of the total aggregate volume V in the reference configuration:

$$\bar{\mathbf{\sigma}} = V^{-1}\int \mathbf{\sigma} dV. \tag{34}$$

Figure 2 shows the model predictions for an aggregate of 300 initially randomly oriented crystals, deformed under uniaxial stress conditions at constant compressive strain rates of $\dot{\varepsilon} = 3500/\text{s}$ and $\dot{\varepsilon} = 8100/\text{s}$. In coincident reference and spatial coordinates, the total deformation gradient is prescribed by $f^1_{.1} = 1 - \dot{\varepsilon} t$ where $\dot{\varepsilon}$ is a constant and the logarithmic strain is $\varepsilon = -\ln f^1_{.1}$. Also shown in Figure 2 is the smoothed experimental stress-strain response obtained from a compressive split Hopkinson bar experiment (Ravichandran, 2007) at a rate of $\dot{\varepsilon} = 8100/\text{s}$. The compressive stress in Figure 2 is the only nonzero component of the average stress of (34), and is labelled as $\bar{\sigma} = \bar{\sigma}^{11}$. In the simulations of Figure 2, grains in the material are specified as randomly oriented since after final heat treatments, quenching and aging, Al 2139 plates are not substantially cold worked or rolled to yield a preferential texture (Cho and Bes, 2006), though experimental texture analysis would provide a stronger justification for the modelling assumption of initially random orientations. Three hundred was found to be a sufficient number of grains to provide an isotropic stress-strain prediction that did not vary substantially with further increases in the number of crystals.

Figure 2 Average compressive stress versus logarithmic compressive strain: experiment and polycrystal model

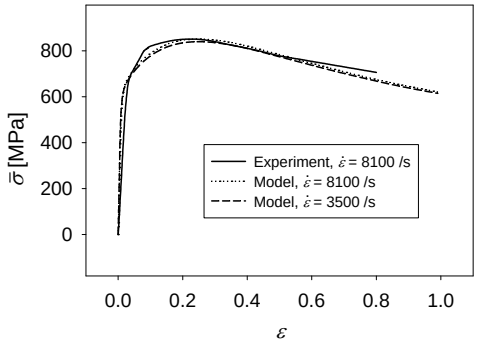

In high-rate experiments (Ravichandran, 2007) variations in strain rate from ~10^3/s to ~10^4/s produced little changes in flow stress, implying that the deviatoric strength of Al 2139 is relatively rate independent over this range of strain rates. The rate independence is manifested in the crystal plasticity model via the large value of m entering (22) and Table 1, and is demonstrated by the close agreement in stress predictions at rates of $\dot{\varepsilon} = 3500/\text{s}$ and $\dot{\varepsilon} = 8100/\text{s}$ in Figure 2. Plasticity model parameters $g_y^{(\alpha)}$, A, B and p are selected in order to obtain the consistency between model and experiment demonstrated in Figure 2, with Φ of (25) taken as zero by default. Notice that the material exhibits a peak compressive strength on the order of 850 MPa at a logarithmic compressive strain of approximately 0.35. Subsequently, stress relaxation occurs, emerging in the model via

both dynamic recovery in (25) and thermal softening in (23). The latter phenomenon occurs as plastic work is converted to temperature rise in adiabatic analyses via (28).

Figure 3 Projectile-plate geometry in simple plugging scenario, with rolling coordinate system

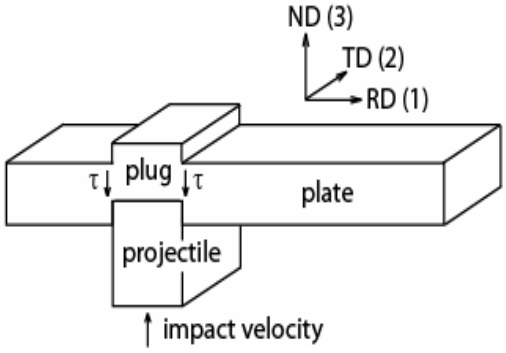

Table 2 Ideal textures for rolled FCC crystals

Texture	$\{hkl\}\langle uvw\rangle$	*Euler angles* $\hat{\psi},\hat{\theta},\hat{\phi}$
Cubic	$\{001\}\langle 100\rangle$	0, 0, 0
Copper	$\{112\}\langle 11\bar{1}\rangle$	180, 35, 135
S	$\{123\}\langle 63\bar{4}\rangle$	211, 37, 117
Brass	$\{110\}\langle \bar{1}12\rangle$	35, 90, 135
Goss	$\{110\}\langle 001\rangle$	0, 90, 135
{100}	$\{001\}\langle ran\rangle$	Random, 0, 0

The crystal model is next used to predict the response to high-rate shearing deformation, specifically resistance to shearing in the direction tangential to the lateral impactor-plate interface occurring during the plug formation and slippage portions of perforation. As shown in Figure 3, this shear stress component σ^{13} is labelled simply as τ. Also shown in Figure 3 is the coordinate system typically used to describe rolled textures (Randle and Engler, 2000), with RD denoting the rolling direction X^1, TD denoting the transverse direction X^2 and ND denoting the normal direction X^3. In addition to the ensemble of 300 randomly oriented grains described already, five single crystalline orientations corresponding to textures obtained during conventional rolling operations on plates or sheets of FCC metals were investigated: cubic, copper, S, brass and Goss textures. The corresponding crystallographic orientations, specifically the Euler angles $(\hat{\psi},\hat{\theta},\hat{\phi})$ in Roe's notation, are listed in Table 2, following Wenk and Van Houtte (2004). In Table 2, $\{hkl\}$ denotes the crystallographic plane normal aligned in the normal direction ND, and $\langle uvw\rangle$ denotes the crystallographic direction aligned parallel to the rolling direction RD. The sixth texture listed in Table 2, labelled as {100}, consists of 300 grains with one

cube axis aligned parallel to the ND, but with the other two cube axes randomly rotated about the ND. This provides for transversely isotropic symmetry in the {100} microstructure, in contrast to the other more conventional rolling textures that generally exhibit orthorhombic symmetry (Wenk and Van Houtte, 2004).

Figure 4 shows adiabatic shear stress-strain behaviour for the randomly oriented and textured Al 2139 crystals. Shearing is conducted in the one to three plane, i.e., $f^1_{.3} = 1 + \dot{\gamma} t$. The macroscopic accumulated shear strain is then found simply as $\gamma = \dot{\gamma} t$, while the average shear stress $\bar{\tau} = V^{-1} \int \sigma^{13} dV$. The prescribed strain rate of $\dot{\gamma} = 10^4$/s is a magnitude typically observed during dynamic perforation (Schoenfeld and Kad, 2002; Clayton, 2005a). From Figure 4, crystals with cubic orientation are predicted to offer substantially greater resistance to shear deformation than the other textures at strains $\gamma < 0.6$, while conversely, crystals with copper orientation are predicted to offer substantially less resistance to shear deformation at strains $\gamma < 0.3$. The aggregate with {100} texture exhibits slightly less shear strength than the cubic texture, but is still substantially stiffer than the remaining cases for $\gamma < 0.6$. It should be noted that the predictions for various textures are not obtained via calibration to experimental data on single crystal orientations since such data remains unavailable for Al 2139; hence, some uncertainty exists in the predictions of Figure 4. Instead, as explained above, the model parameters are calibrated to polycrystal data assuming random orientations (Figure 2), and differences in response among different textures then arise naturally in the computations as a result of elastic and plastic anisotropy, the latter induced by initial and evolving orientations of the slip directions.

Figure 4 Average shear stress versus shear deformation at $\dot{\gamma} = 10^4$/s: polycrystal model with initial textures

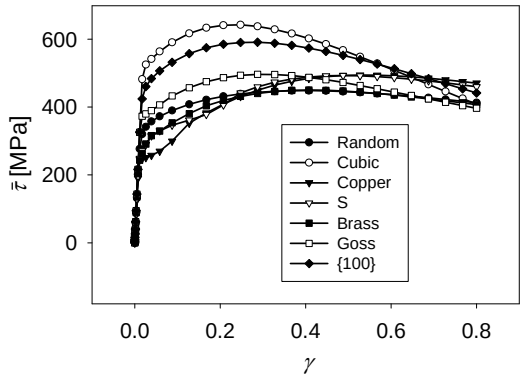

In what follows next, thermomechanical behaviours of eight different microstructures, corresponding to eight sets of crystal parameters – specifically variations in texture, hardening rate and residual energy storage – are investigated. Microstructures and parameters are listed in Table 3. Microstructures 1 and 5–8 feature random textures with 300 grains, while microstructures 2 and 3 feature cubic and copper textures, respectively, corresponding to the stiffest and most compliant orientations with respect to high-rate shearing as indicated in Figure 4. Microstructure 4, an aggregate of 300 grains randomly

oriented about the ND axis ({100} orientation), is also studied. Microstructures 5 and 6 include nonzero values of Φ, with microstructure 5 corresponding to a 50% increase in the rate of hardening associated with the first term on the right of (25), and microstructure 6 corresponding to a 50% reduction in this rate of hardening. Differences in hardening rates may be attributed to various concentrations of alloying ingredients in Al-Cu-Mg alloys leading to different solutions and precipitate distributions, for example, as discussed by Starink et al. (1999), Hutchinson et al. (2001) and Cho and Bes (2006). Note that the material is not considered free of precipitates or associated lattice defects when $\Phi = 0$. The value $\Phi = 0$ is used as only as a relative reference, with enhancement of strain hardening due to such defects represented by $\Phi > 0$, and reduction in hardening represented by $\Phi < 0$. Finally, microstructures 7 and 8 exhibit, through nonzero values of Ω, increased energy storage capacity. As will be shown later, positive values of Ω result in smaller values of the heat dissipation fraction β of (29) and (32), leading to less adiabatic heating than would occur for otherwise equivalent microstructures with $\Omega = 0$. As mentioned already, stress concentrations at phase boundaries as well as residual stresses supported directly by second-phase particles in Al-Cu-Mg-Ag alloys presumably may contribute to variations in Ω.

Table 3 Microstructures investigated in polycrystalline and macroscopic simulations

Microstructure	*Texture*	Φ	Ω
1	Random	0.0	0.0
2	Cubic	0.0	0.0
3	Copper	0.0	0.0
4	{100}	0.0	0.0
5	Random	1.5	0.0
6	Random	0.5	0.0
7	Random	0.0	1.0
8	Random	0.0	2.0

Average effective stress-shear strain behaviours for polycrystalline aggregates corresponding to the eight cases of Table 3 are shown in Figure 5. Again the prescribed deformation is pure shear, $f^1_{.3} = 1 + \dot{\gamma} t$, at a constant rate of $\dot{\gamma} = 10^4$/s. The effective Cauchy stress follows the usual definition:

$$\bar{\sigma} = \frac{1}{\sqrt{2}} \left\{ \left(\bar{\sigma}^{11} - \bar{\sigma}^{22} \right)^2 + \left(\bar{\sigma}^{22} - \bar{\sigma}^{33} \right)^2 + \left(\bar{\sigma}^{33} - \bar{\sigma}^{11} \right)^2 + 6 \left[\left(\bar{\sigma}^{12} \right)^2 + \left(\bar{\sigma}^{23} \right)^2 + \left(\bar{\sigma}^{31} \right)^2 \right] \right\}^{1/2}, \quad (35)$$

with individual stress components on the right side of (35) following from volume integral (34). Note that (35) is consistent with the notation used in Figure 2, since the effective stress and the normal stress are equal under the uniaxial conditions considered in Figure 2. Note also that the shear stress definition used in Figure 4 and the effective stress of definition (35) are related by $\bar{\sigma} = \sqrt{3}\bar{\tau}$. From Figure 5, the following observations are made. Microstructures 2 and 4 exhibit the largest shear strengths (i.e., flow stresses) at strains $\gamma < 0.4$ due to respective cubic and {100} orientations, and microstructure 5 exhibits the largest shear strength at strains $\gamma > 0.4$ due to the prescribed increased hardening rate. Microstructure 3 exhibits the lowest shear strength among all

cases at strains $\gamma < 0.17$, because of its copper texture, while microstructure 6 exhibits the lowest shear strength at larger strains $\gamma > 0.17$ because of its prescribed reduced hardening rate. Microstructures 7 and 8 demonstrate slightly higher flow stresses than the base microstructure 1, because of the reductions in temperature rise and correspondingly reduced thermal softening in the former. Recall that in microstructures 7 and 8, increased energy storage leads to less dissipation and less adiabatic temperature rise. For microstructure 7, the increase in flow stress relative to microstructure 1 begins to emerge at $\gamma \approx 0.2$, while such increases emerge slightly sooner in the deformation history, at strains around $\gamma \approx 0.17$, for microstructure 8.

Figure 5 Average effective stress versus shear deformation at $\dot{\gamma} = 10^4/\text{s}$: polycrystal model with various microstructural parameters

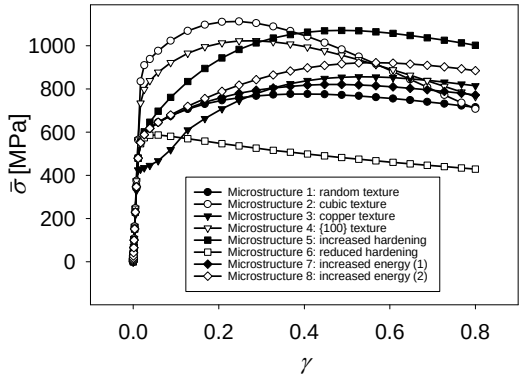

Figure 6 Average ratio of net dissipated energy to plastic work versus shear deformation at $\dot{\gamma} = 10^4/\text{s}$: polycrystal model with various microstructural parameters

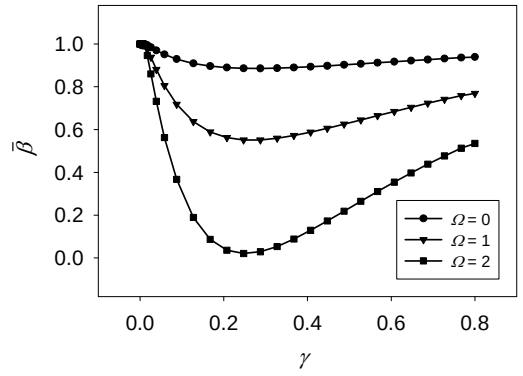

Thermodynamics of energy storage are investigated in more detail in Figure 6. Considered in Figure 6 are microstructures 1, 7 and 8 of Table 3, corresponding to randomly oriented polycrystals with values of Ω of 0, 1 and 2, respectively. The results

correspond to the same high-rate simulations described in Figure 5. The average heat dissipation fraction shown in Figure 6 is computed from:

$$\overline{\beta} = V^{-1} \int \beta dV, \tag{36}$$

where the local value of β for each crystal of the aggregate follows from (32).

For microstructure 1 with Ω = 0, a range of $0.8 < \overline{\beta} \leq 1.0$ over the strain history is obtained, a range typically observed and/or assumed for many FCC metals undergoing significant plastic deformation (Taylor and Quinney, 1934; Aravas et al., 1990). Such a result is used to motivate the choice of the value of κ listed in Table 1. For microstructure 7 with Ω = 1, the lower bound of $\overline{\beta}$ drops relative to that of microstructure 1 such that $0.55 \leq \overline{\beta} \leq 1.0$ over the deformation history in the former. For microstructure 8 with Ω = 2, the lower bound drops even further and $0.02 \leq \overline{\beta} \leq 1.0$. In each case, the predicted value of $\overline{\beta}$ decreases initially with strain as dislocations accumulate in conjunction with hardening mechanisms, leading to an increased rate of energy storage associated with self-equilibrated internal stress fields supported by the defects. Then at larger strains γ > 0.3, an increase in $\overline{\beta}$ with strain is observed as the rate of dislocation accumulation slows due to dynamic recovery prescribed in (25). Similar trends and ranges of $\overline{\beta}$ falling between bounds predicted here for Ω = 1 and Ω = 2, have been observed in rate-insensitive alloy Al 2024-T351 (Rosakis et al., 2000).

4 Macroscopic model formulation and calibration

A macroscopic thermoviscoplastic model is implemented for use in impact simulations of a steel cylinder striking a monolithic flat plate of the Al 2139 alloy. The macroscopic plasticity model parameters for the Al plate are calibrated repeatedly to stress-strain results from the polycrystal model shown in Figure 5, with a different set of parameters obtained for each microstructural feature that is varied among simulations listed in Table 3: hardening rate, energy storage rate, or texture. The macroscopic damage model for the Al plate is calibrated to experimental observations of tensile and compressive failure for use in most of the impact simulations. However, effects of variable ductility of the Al plate on its dynamic performance are also studied via systematic adjustment of the damage model's parameters. The macroscopic framework also relies upon a Mie-Gruniesen equation of state (Johnson et al. 1997) providing the relationship between volumetric strain, pressure and temperature and accounting for elastic nonlinearity at high pressures. In a certain sense, the deviatoric plasticity component of the present work can be considered multiscale since macroscopic parameters emerge from finer scale, crystal plasticity modelling, while the volumetric response and damage model are purely macroscopic in origin.

The viscoplastic response follows from an associated flow rule whereby the radius of the isotropic yield surface, in terms of scalar deviatoric stress measure (35), is given by:

$$\overline{\sigma} = \left[Y_0 + Y_1 \varepsilon_p^N \right] \left[1 - \left(\theta / \theta_1 \right)^M \right], \tag{37}$$

with Y_0 the initial yield stress, ε_p the cumulative equivalent plastic strain, and other nonzero material constants Y_1, N and M reflecting linear and exponential strain hardening and thermal softening, respectively. Fundamentally different forms of flow rules have been suggested in (22)–(23) and (37). Either type of rule is sufficient to reproduce the limited experimental data. The microscopic flow rule of Section 2 was developed for anisotropic single crystals, while the macroscopic rule of Section 4 is appropriate only for isotropic polycrystals. The simple macroscopic rule (37) is chosen here for computational efficiency, without stringent regard for the physics of plastic deformation. More complex models with a stronger basis in physics are available (Wright, 2002), but the limited amount of experimental data that exist for Al 2139 is insufficient to enable unique selection of all parameters entering more detailed models.

The three-dimensional implementation features an additive decomposition of the spatial deformation rate into elastic and deviatoric plastic parts, and explicit numerical integration using a radial return algorithm with the Jaumann rate of Cauchy stress taken as the objective rate. Additional details regarding the numerical implementation, mostly standard in the computational plasticity literature, can be found in Johnson et al. (1997). In the implementation of the macroscopic model, energy equation (18) is simplified as:

$$\rho \hat{c} \dot{\theta} = \bar{\beta} \boldsymbol{\sigma} : \mathbf{l}^{\mathbf{p}} + \varsigma, \tag{38}$$

where $\mathbf{l}^{\mathbf{p}}$ is the spatial plastic velocity gradient (or the plastic strain rate since $\boldsymbol{\sigma} = \boldsymbol{\sigma}^T$), $\bar{\beta}$ is a constant, and the function ς accounts for temperature changes manifesting from the equation of state.

In simulations of impact events involving large deformations, failure models are typically needed to capture the loss of strength commensurate with shear localisation, fracture, or spall. In the model implemented here, damage is assumed to accumulate in the material with cumulative inelastic deformation, with the maximum tolerable amount of damage accumulation increasing with the stress triaxiality; i.e., damage accumulation is accelerated by tensile pressure and retarded by compressive pressure. Upon failure, the mass of the material is conserved, but the solid is presumed to no longer support deviatoric stress or tensile hydrostatic stress. The cumulative inelastic strain ε_P at which failure occurs is:

$$\varepsilon_p^f = D_0 f(\theta) \exp(D_1 p / \bar{\sigma}), \tag{39}$$

where D_0 is the failure strain under conditions of pure shear, and D_1 accounts for increases (decreases) in ductility with increasing (decreasing) pressure $p = -tr(\boldsymbol{\sigma})/3$. Finally, f accounts for possible effects of temperature on ductility. In the numerical implementation, (39) is used in an incremental form since the local pressure and deviatoric stress state may vary with the time history of deformation. Note that more elaborate and physically descriptive plasticity and damage models could lend more realism to the macroscopic simulations when sufficient experimental data become available to populate the extensive parameter sets of more complex models. Because sufficient data are not available to calibrate f for Al 2139, here $f = 1$ is used in all simulations, regardless of microstructure.

In the impact simulations that follow, values of parameters entering (37)–(39) are varied in order to reflect microstructures modelled explicitly with crystal plasticity theory in Section 3. As listed in Table 4, values of parameters entering (37) are varied in

calibrations of the macroscopic plasticity model to the high-rate results of Figure 5, assuming a stress state of pure shear. Recall that the material was found to be fairly rate insensitive over the range of high strain rates of present interest; hence the absence of strain rate effects on hardening in (37) is thought justified. In simulations 1–8, constants corresponding to weighted averages of $\bar{\beta}$ introduced in (36) over the deformation history are used in (38), with emphasis given to values at strains prior to failure $\gamma < 0.3$. Values of Y_0, Y_1, N and M are then chosen such that the results of (37) and (38) best fit the polycrystal plasticity predictions of Figure 5.

Table 4 Simulations, microstructures and corresponding macroscopic model parameters

Sim. #	*Microstructure*	Y_0*(MPa)*	Y_1*(MPa)*	N	M	$\bar{\beta}$	D_0	D_1
1	1	610	2,250	0.23	1.10	0.945	0.3	2.0
2	2	300	3,000	0.10	1.30	0.954	0.3	2.0
3	3	300	3,500	0.40	1.20	0.947	0.3	2.0
4	4	250	3,000	0.15	1.40	0.952	0.3	2.0
5	5	100	4,000	0.30	1.40	0.838	0.3	2.0
6	6	1,630	125	0.20	0.80	0.999	0.3	2.0
7	7	610	2,250	0.26	1.23	0.790	0.3	2.0
8	8	610	2,600	0.30	1.20	0.552	0.3	2.0
9	1	610	2,250	0.23	1.10	0.945	0.45	2.0
10	1	610	2,250	0.23	1.10	0.945	0.15	2.0

For microstructures featuring randomly oriented grains, use of an isotropic material model is deemed acceptable, at least for monotonic (as opposed to cyclic) deformation scenarios where directional back-stresses need not be delineated. However, for microstructures 2–4, the shearing response of plastically anisotropic crystals is used to calibrate an isotropic macroscopic model. Such an assumption may over- or under-estimate the deviatoric strength of the material in other directions. On the other hand, if the shearing response dominates resistance to perforation and plugging as has been suggested elsewhere (Li and Goldsmith, 1996; Schoenfeld and Kad, 2002), the use of an isotropic macroscopic model to compute the resistance of textured sheets to penetration may at least provide reasonable bounds on performance that suggest directions for material improvements, if not precise results. More realistic results for textured sheets could presumably be attained by calibration of the crystal predictions to an anisotropic macroscopic theory, for example one featuring an orthotropic yield surface (Hill, 1949). Finally, for cylindrical projectiles of the sort considered here, shear stresses resisting penetration may be non-uniform along the circumference of the projectile-target interface for rolling textures lacking transverse isotropy. Hence, the results reported for the sheet with transversely isotropic {100} texture (simulation 4) are thought to provide a more realistic prediction of performance for a rolled sheet with cubic texture than those of simulation 2 that assume all shear stresses occur tangential to {001} planes in the lattice.

Remaining material parameters are selected as follows. In simulations 1–8, values of D_0 and D_1 are chosen based on experimental observations (Cho and Bes, 2006; Ravichandran, 2007) that the Al 2139 exhibits a tensile elongation of ~0.15, a shear

ductility of ~0.3, and a compressive ductility in excess of 0.5. In simulations 9 and 10, respectively, the ductility of the material is increased or decreased by a factor of 0.5, in order to quantify effects of ductility on simulated performance. Library parameters typical for aluminium alloys (Kohn, 1969) are used for the macroscopic equation of state of Al 2139, details of which are available elsewhere (Johnson et al., 1997). Possible affects of variations of microstructure on the hydrostatic response are not addressed.

The above discussion pertains to the modelling of the target Al plate. The steel projectile's behaviour is modelled identically in all simulations, using standard appropriate versions of (37)–(39) accounting for high strain rate effects on plasticity and fracture, an equation of state for the volumetric response, and available macroscopic library parameters for 4340 steel (Kohn, 1969; Johnson and Cook, 1983, 1985). Also for the steel, the default $\overline{\beta} = 1$ is used in (39).

5 Impact simulations

The simulations considered here involve a projectile comprised of 4340 steel, impacting a square Al 2139 plate of 19.05 mm (0.75") thickness. The projectile is modelled as a right circular cylinder (Gama et al., 2001), of diameter 20 mm, length 22 mm and mass 53.7 g. The lateral dimensions of the plate are an order of magnitude greater than its thickness, i.e., 190.5 mm × 190.5 mm. The large lateral dimensions ensure that the perforation process concludes before stress wave reflections from the boundaries affect the behaviour of the projectile. The initial velocity of the projectile in all simulations is specified as 1,000 m/s, perpendicular to the surface of the target (i.e., null obliquity). The performance metric chosen here is the residual velocity v_R of the projectile after perforation: the smaller the residual velocity, the better the performance of the plate. The present approach, in which the plate is severely overmatched by the projectile, renders quantitative performance appraisal more straightforward, via consideration of v_R, than would be the case if perforation did not occur in all instances. This approach also reduces possible dependence of the solution on mesh density that may become excessive as the limit velocity approaches zero. In order to obtain a precise, mesh-independent prediction of the limit velocity, a constitutive and numerical formulation including an intrinsic length scale of dimension larger than the grid spacing should be used, for example one resolving microstructural features or incorporating spatial gradients of field variables such as plastic deformation or damage (Voyiadjis and Abu Al-Rub, 2006).

Several mesh densities were considered, with only half of the full geometry represented as permitted by symmetry reductions. The performance metric v_R was found to be nearly insensitive to the number of nodes and elements in the mesh at the chosen mesh density, consisting of a total of 138,240 tetrahedral elements. A dynamic Lagrangian analysis package was used, with default values for parameters controlling time integration, artificial viscosity and element-to-particle conversion (Johnson et al. 1997). Regarding the latter, in order to obviate problems encountered with large element distortions, finite elements undergoing very large deformations, i.e., effective strains greater than 0.5, are converted, via a mass-conservative transformation, to a meshless environment with a generalised particle algorithm (Johnson et al., 2000).

Results from simulation 1 of Table 4 are visualised in Figure 7, at four time instances of the impact event. The steel cylinder clearly undergoes large compressive deformation

along its axial direction, and lateral expansion in the vicinity of the impact face. Plugging failure of the aluminium plate is also observed, with the velocity of the plug clearly exceeding that of the projectile at t = 300 μs in Figure 7(d). In addition to the primary plug, a debris cloud of smaller fragments of the Al alloy is also visible behind the plate. The results depicted in Figure 7 for simulation 1 are qualitatively similar to those observed in the other cases listed in Table 4.

Figure 7 Simulation of perforation of microstructure 1 at (a) t = 0 (b) t = 20 μs (c) t = 100 μs (d) t = 300 μs

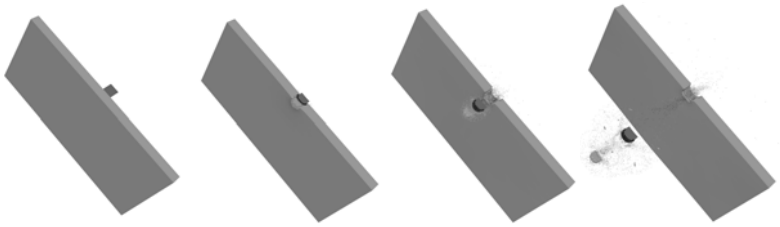

(a) (b) (c) (d)

Figure 8 Average final residual velocities of projectile for ten simulations corresponding to ten different hypothetical microstructures of the Al 2139 plate

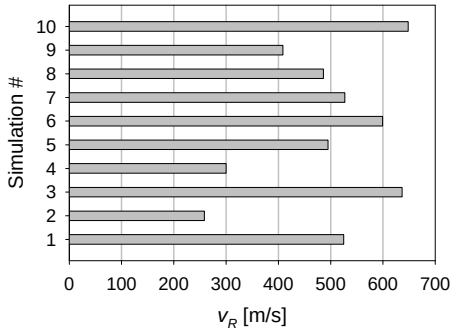

Residual velocities for all nine simulations are shown in Figure 8. These are obtained from the solution data via the spatial integral:

$$v_R = \hat{V}^{-1} \int v_3 d\hat{V}, \tag{40}$$

with $\hat{V}$ the instantaneous (i.e., current configuration) volume of the projectile and v_3 the component of the velocity vector in the normal direction (ND) to the plate, as introduced in Figure 3. Residual velocities remained relatively constant at simulation times t > 1300 μs, though the values shown in Figure 8 correspond to the instant t = 300 μs. Recall that each simulation corresponds to a different set of material parameters (Table 4) associated with variations in microstructure (Table 3). The baseline result for comparison with the other cases is simulation 1, featuring isotropic properties corresponding to a random set

of grain orientations, with strength and ductility calibrated most closely to available experimental data (Cho and Bes, 2006; Ravichandran, 2007). For simulation 1, v_R = 525 m/s.

In general, the greater the strength or ductility of the plate, the more energy absorbed by the plate during impact and perforation, the greater the reduction in kinetic energy of the cylindrical projectile, and lower the cylinder's residual velocity. Simulations 2 and 4 exhibit very low residual velocities, v_R = 258 m/s and v_R = 300 m/s, respectively, as a result of increased shear strengths attributed to texturing. These correspond to microstructures 2 and 4 of Figure 5.

Because of its high hardening rate, simulation 5 also exhibits a lower residual velocity than case 1, v_R = 495 m/s, though the reduction in residual velocity is not as drastic as for simulations 2 and 4 because the largest increases in strength in simulation 5 manifest only at large strains, visible in Figure 5 for microstructure 5 with $\gamma > 0.4$. According to (39) and the failure model parameters used here, such large strains are not sustainable by the material unless the stress state is highly compressive. In the present simulations, the material tends to lose strength and energy absorbing capacity prior to realisation of the increased strength that would be afforded at very high pressures.

Simulations 3 and 6 suffer degradation in performance relative to base simulation 1 because of their reduced shear strengths, translating to a reduction in kinetic energy mitigation of the plate. Recall from Figure 5 that in simulation 3 the strength is reduced due to lattice orientation effects, while in simulation 6 the strength is reduced due to a decreased hardening rate associated with composition, e.g., solution effects or second-phase particle content and morphology. As such, the residual velocities are relatively high: in simulation 3, v_R = 637 m/s and in simulation 6, v_R = 599 m/s.

Simulations 7 and 8 offer the possibility of improved dynamic performance of the Al 2139 alloy via an increase in the material's ability to store residual elastic energy. In these cases, increases in residual elastic energy result in a decrease in the adiabatic temperature rise, leading to increased strength since thermal softening and shear localisation processes (Wright, 2002) are impeded. However, in the present investigation, simulation 7 yields a comparable residual velocity to simulation 1, since benefits in strength attributed to increased elastic energy storage are small and do not emerge in simulation 7 until relatively large shear strains are attained. Simulation 8, on the other hand, with greater energy storage (Figure 6) and strength increases at lower strains (Figure 5) provides modest improvement in performance relative to case 1, with v_R = 486 m/s.

Finally, effects of ductility are quantified by comparing results from simulations 1, 9 and 10. A 50% increase in ductility, assuming no change in the influence of triaxiality upon failure strain, provides a substantial reduction in residual velocity and a noticeable improvement in performance, with v_R = 409 m/s in simulation 9. Conversely, a 50% decrease in ductility results in an expected increase in residual velocity and inferior performance, with v_R = 648 m/s for simulation 10.

6 Conclusions

A two-scale approach has been implemented to estimate effects of fine scale material parameters on the macroscopic constitutive behaviour of an Al-Cu-Mg-Ag alloy and its resistance to impact and perforation. At the fine scale of resolution, a crystal plasticity

model has been developed, accounting for finite deformations, grain orientation effects and consistent thermodynamics associated with temperature changes, lattice defects and residual elastic energy. Flexibility has been inserted into the model enabling description of the effects of composition on slip system-level hardening and energy storage, for example, attributed to interactions between dislocations and second-phase precipitates. An averaging scheme has been used to obtain macroscopic model parameters corresponding to hypothetical microstructures of Al-Cu-Mg-Ag alloys conceivably attainable via processing operations. Such operations include texturing by rolling or strengthening via addition of alloying ingredients. Macroscopic simulations of impact and perforation of thin plates of the alloy were conducted, and effects upon performance of material properties corresponding to different crystalline microstructures were quantified in terms of residual velocities of the projectile.

The results suggest that the most substantial improvements in dynamic performance of the Al alloy may be achieved by rolling to instil a cubic texture or by taking processing steps to substantially increase the alloy's ductility, e.g., maximum elongation increases on the order of 50%. Additional benefits may be achieved from composition changes that provide increases in rates of slip system hardening, e.g., an increase in strengthening rate on the order of 50%, or increases in the rate energy storage, e.g., a reduction in the average fraction of dissipated plastic work from 0.95 to 0.55. In the present theoretical-computational study, each microstructural variation has been examined in isolation, though property variations are likely highly coupled in physically realistic structure-processing paths. For example, adjustment of strength of the alloy without alteration of its ductility may prove difficult using traditional processing routes. However, the present research provides some quantification of improvements to impact and perforation resistance that could be realised via realistic adjustments to the microstructure of Al 2139, and some guidance as to which microstructure properties and features may be of highest priority when considering the dynamic performance of metallic plates from a micromechanics perspective. Clearly the most substantial benefits would emerge from processing efforts that seek to simultaneously increase strength, ductility and energy storage mechanisms.

It is noted that a number of limitations lend uncertainty to performance predictions of the crystal plasticity model and subsequent macroscopic impact simulations. The crystal plasticity predictions should be viewed as most accurate only for loading conditions for which the model has been calibrated, namely polycrystals deformed in compression, initially at room temperature at strain rates up to approximately 10^4/s. The robustness of the crystal plasticity model, and the quality of the calibration of parameters, could be improved via consideration of additional experimental data obtained for crystals subjected to various stress states, and in various non-random initial orientations. Regarding the ballistic simulations, experimental data used for calibration of deviatoric plasticity parameters and the macroscopic failure model are limited to macroscopic data collected over a range of strain rates up to 10^4/s, even though higher strain rates may be achieved in the target material during the impact event. The macroscopic models used here do not attempt to explicitly resolve the discrete nature of failure mechanisms such as fracture and shear localisation that could be addressed more realistically in a multiscale context (Clayton, 2006) if accompanied by sufficient experimental characterisation. For three of the cases investigated here featuring textured materials, some effects of anisotropy are neglected in the macroscopic model, specifically the stress components

other than that component providing the shear resistance to plugging on planes orthogonal to the rolling direction. Hence, the benefit of cubic texturing (simulation 2) reported in Figure 8 may be overestimated, with the transversely isotropic {100} texture (simulation 4) offering perhaps a more reasonable prediction of the maximum performance improvement attainable via rolling of the Al plate. Nonetheless, the present results do provide previously unavailable guidance as to which micromechanical phenomena should be given high priority when developing alloys for resistance to high velocity impact and perforation.

Acknowledgements

This work was supported by the Joint Improvised Explosive Device Defeat Organization.

References

Aravas, N., Kim, K.S. and Leckie, F.A. (1990) 'On the calculations of the stored energy of cold work', *ASME J. Eng. Mat. Tech.*, Vol. 112, pp.465–470.

Arsenlis, A. and Parks, D.M. (2002) 'Modelling the evolution of crystallographic dislocation density in crystal plasticity', *J. Mech. Phys. Solids*, Vol. 50, pp.1979–2009.

Becker, R. (2004) 'Effects of crystal plasticity on materials loaded at high pressures and strain rates', *Int. J. Plasticity*, Vol. 20, pp.1983–2006.

Brown, L.M. and Stobbs, W.M. (1971) 'Work hardening of copper-silica. 2. Role of plastic relaxation', *Phil. Mag.*, Vol. 23, pp.1201–1233.

Cheeseman, B. (2007) *Private Communication.*

Cheng, W.L. and Itoh, S. (2004) 'High velocity impact of steel fragment on thick aluminium target', *Mater. Sci. Forum*, Vol. 465–466, pp.49–54.

Cho, A. and Bes, B. (2006) 'Damage tolerance capability of an Al-Cu-Mg-Ag alloy (2139)', *Mater. Sci. Forum*, Vol. 519–521, pp.603–608.

Clayton, J.D. (2005a) 'Dynamic plasticity and fracture in high density polycrystals: constitutive modelling and numerical simulation', *J. Mech. Phys. Solids*, Vol. 53, pp.261–301.

Clayton, J.D. (2005b) 'Modelling dynamic plasticity and spall fracture in high density polycrystalline alloy', *Int. J. Solids Structures*, Vol. 42, pp.4613–4640.

Clayton, J.D. (2006) 'Continuum multiscale modelling of finite deformation plasticity and anisotropic damage in polycrystals', *Theo. Appl. Fract. Mech.*, Vol. 45, pp.163–185.

Dwivedi, S.K., Asay, J.R. and Gupta, Y.M. (2006) 'Two-dimensional mesoscale simulations of quasi-elastic reloading and unloading in shock compressed aluminium', *J. Appl. Phys.*, Vol. 100, 083509.

Gall, K., Horstemeyer, M., McDowell, D.L. and Fan, J. (2000) 'Finite element analysis of the stress distributions near damaged Si particle clusters in cast Al-Si alloys', *Mech. Mater.*, Vol. 32, pp.277–301.

Gama, B.A., Bogetti, T.A., Fink, B.K., Yu, C-Y., Claar, T.D., Eifert, H.H. and Gillespie, J.W. (2001) 'Aluminium foam integral armor: a new dimension in armor design', *Composite Struct.*, Vol. 52, pp.381–395.

Hanim, S. and Klepaczko, J.R. (1999) 'Numerical study of spalling in an aluminium alloy 7020-T6', *Int. J. Impact Eng.*, Vol. 22, pp.649–673.

Hatch, J.E. (1984) 'Aluminium properties and physical metallurgy', *American Society for Metals*, Metals Park, OH.

Hill, R. (1949) 'Constitutive modelling of orthotropic plasticity in sheet metals', *ASME J. Appl. Mech.*, Vol. 16, pp.349–357.

Hutchinson, C.R., Fan, X., Pennycook, S.J. and Shiflet, G.J. (2001) 'On the origin of the high coarsening resistance of Ω plates in Al-Cu-Mg-Ag alloys', *Acta Mater*, Vol. 49, pp.2827–2841.

Johnson, G.R. and Cook, W.H. (1983) 'A constitutive model and data for metals subjected to large strains, high strain rates, and high temperatures', *Proc. 7th Int. Symp. on Ballistics*, The Hague, Netherlands, pp.541–547.

Johnson, G.R. and Cook, W.H. (1985) 'Fracture characteristics of three metals subjected to various strains, strain rates, temperatures, and pressures', *Eng. Fract. Mech.*, Vol. 21, pp.31–48.

Johnson, G.R., Beissel, S.R. and Stryk, R.A. (2000) 'A generalized particle algorithm for high velocity impact calculations', *Computational Mech.*, Vol. 25, pp.245–256.

Johnson, G.R., Stryk, R.A., Holmquist, T.J. and Beissel, S.R. (1997) 'Numerical algorithms in a Lagrangian hydrocode', AFWL-TR-1997-7039, Eglin Air Force Base, FL, approved for public release.

Kalidindi, S.R., Bronkhorst, C.A. and Anand, L. (1992) 'Crystallographic texture evolution in bulk deformation processing of FCC metals', *J. Mech. Phys. Solids*, Vol. 40, pp.537–569.

Kocks, U.F., Argon, A.S. and Ashby, M.F. (1975) 'Thermodynamics and kinetics of slip', *Prog. Mater. Sci.*, Vol. 19, pp.1–281.

Kohn, B.J. (1969) 'Compilation of Hugoniot equations of state', AFWL-TR-1969-38, Kirtland Air Force Base, NM, approved for public release.

Li, K.Z. and Goldsmith, W. (1996) 'A phenomenological model for perforation of moderately thick plates by tumbling projectiles', *Int. J. Solids Structures*, Vol. 33, pp.3561–3575.

Mott, N.F. and Nabarro, F.R.N. (1948) 'Report of Bristol conference on the strength of solids', *The Physical Society*, pp.1–18, London.

Povrik, G.L., Mohan, R. and Brown, S.B. (1995) 'Crystal plasticity simulations of thermal stresses in thin-film aluminium interconnects', *J. Appl. Phys.* Vol. 77, pp.598–606.

Randle, V. and Engler, O. (2000) *Introduction to Texture Analysis: Macrotexture, Microtexture, and Orientation Mapping*, Gordon and Breach Scientific Publishers, Australia.

Ravichandran, G. (2007) *Private Communication.*

Rezvanian, O., Zikry, M.A. and Rajendran, A.M. (2006) 'Microstructural modelling of grain subdivision and large strain inhomogeneous deformation modes in FCC crystalline materials', *Mech. Mater.*, Vol. 38, pp.1159–1169.

Rosakis, P., Rosakis, A.J., Ravichandran, G. and Hodowany, J. (2000) 'A thermodynamic internal variable model for the partition of plastic work into heat and stored energy in metals', *J. Mech. Phys. Solids*, Vol. 48, pp.581–607.

Schoenfeld, S.E. and Kad, B.K. (2002) 'Texture effects on shear response in Ti-6Al-4V plates', *Int. J. Plasticity*, Vol. 18, pp.461–486.

Starink, M.J., Wang, P., Sinclair, I. and Gregson, P.J. (1999) 'Microstructure and strengthening of Al-Li-Cu-Mg alloys and MMCs: II. Modelling of yield strength', *Acta Mater*, Vol. 47, pp.3855–3868.

Taylor, G.I. (1938) 'The mechanism of plastic deformation of crystals', Proc. *R. Soc.A*, London, Vol. 145, pp.362–415.

Taylor, G.I. and Quinney, H. (1934) 'The latent energy remaining in a metal after cold working', *Proc. R. Soc. A*, London, Vol. 143, pp.307–326.

Vasudevan, A.K., Ludwiczak, E.A., Baumann, S.F., Howell, P.R., Doherty, R.D. and Kersker, M.M. (1986) 'Grain-boundary fracture in Al-Li alloys', *Mater. Sci. Tech.*, Vol. 2, pp.1205–1209.

Voyiadjis, G.Z. and Abu Al-Rub, R.K. (2006) 'A finite strain plastic-damage model for high velocity impacts using combined viscosity and gradient localization limiters: part II–numerical aspects and simulations', *Int. J. Damage Mech.*, Vol. 15, pp.335–373.

Wenk, H-R. and Van Houtte, P. (2004) 'Texture and anisotropy', *Rep. Prog. Phys.*, Vol. 67, pp.1367–1428.

Wright, T.W. (2002) *The Physics and Mathematics of Adiabatic Shear Bands*, Cambridge Univ. Press, Cambridge.

Wu, Y-Q., Shi, H-J., Zhang, K-S. and Yeh, H-Y. (2006) 'Numerical investigation of grain boundary effects on elevated-temperature deformation and fracture', *Int. J. Solids Structures*, Vol. 43, pp.4546–4577.

Zhao, Z., Radovitzky, R. and Cuitino, A. (2004) 'A study of surface roughening in FCC metals using direct numerical simulation', *Acta Mater*, Vol. 52, pp.5791–5804.

NO. OF
COPIES ORGANIZATION

1 (PDF only) DEFENSE TECHNICAL INFORMATION CTR
DTIC OCA
8725 JOHN J KINGMAN RD
STE 0944
FORT BELVOIR VA 22060-6218

1 DIRECTOR
US ARMY RESEARCH LAB
IMNE ALC HRR
2800 POWDER MILL RD
ADELPHI MD 20783-1197

1 DIRECTOR
US ARMY RESEARCH LAB
RDRL CIM L
2800 POWDER MILL RD
ADELPHI MD 20783-1197

1 DIRECTOR
US ARMY RESEARCH LAB
RDRL CIM P
2800 POWDER MILL RD
ADELPHI MD 20783-1197

1 DIRECTOR
US ARMY RESEARCH LAB
RDRL D
2800 POWDER MILL RD
ADELPHI MD 20783-1197

ABERDEEN PROVING GROUND

1 DIR USARL
RDRL CIM G (BLDG 4600)

NO. OF
COPIES ORGANIZATION

ABERDEEN PROVING GROUND

19 DIR USARL
RDRL WMM B
B CHEESEMAN
RDRL WMP B
J CLAYTON (15 CPS)
C HOPPEL
RDRL WMP C
T BJERKE
RDRL WMP F
N GNIAZDOWSKI

INTENTIONALLY LEFT BLANK.